Efficient degradation of PPCPs by $Mo_{1-x}S_{2-y}$ with S vacancy at phase-junction: Promoted by innergenerate-H_2O_2

Xiaojuan Bai [a,b,*], Xuyu Wang [a], Tianqi Jia [a], Linlong Guo [a], Derek Hao [c], Ziyang Zhang [a], Liyuan Wu [a], Xiaoran Zhang [a], Hua Yang [a], Yongwei Gong [a], Junqi Li [a], Haiyan Li [a,**]

[a] *Key Laboratory of Urban Stormwater System and Water Environment (Beijing University of Civil Engineering and Architecture), Ministry of Education, Beijing 100044, China*
[b] *Beijing Engineering Research Center of Sustainable Urban Sewage System Construction and Risk Control, Beijing University of Civil Engineering and Architecture, Beijing 100044, China*
[c] *Centre for Catalysis and Clean Energy, Gold Coast Campus, Griffith University, Gold Coast 4222 Australia*

ARTICLE INFO

ABSTRACT

Currently, inner-generate hydrogen peroxide to enhance the degradation of pollutants is an outstanding way. However, few studies have been done on MoS$_2$ photocatalysts with sulfur vacancies at the phase-junction to produce innergenerate-H$_2$O$_2$ to promote contaminants degradation. Herein, we prepared Mo$_{1-x}$S$_{2-y}$ photocatalysts with sulfur vacancies at the phase-junction by a simple method (temperature-programmed reduction in hydrogen atmosphere) to achieve high innergenerate-H$_2$O$_2$ and high degradation efficiency. Specifically, Mo$_{1-x}$S$_{2-y}$ exhibited a high yield of innergenerate-H$_2$O$_2$ (35 μmol L^{-1} h^{-1}, 1.5 times as high as bulk MoS$_2$) under simulated solar irradiation, because the promoted electron transfer can increase superoxide radical to generate innergenerate-H$_2$O$_2$. Hydroxyl radicals generated by decomposition of innergenerate-H$_2$O$_2$ through the transformation of variable metal molybdenum atom (Mo(IV)/Mo(VI)) can effectively improve the degradation efficiency of tetracycline and diclofenac sodium (twice as high as bulk MoS$_2$). The novel and concise way was paved to synthesize photocatalysts for high-efficiency photocatalytic degradation by innergenerate-H$_2$O$_2$.

1. Introduction

Over the past decade, owing to the emission situation, the water environment is continually polluted by pharmaceuticals and personal care products (PPCPs) such as antibiotics, which would observably deteriorate the health state of humans due to their characteristics of difficult degradation [1–5]. Therefore, emission control and removal of antibiotics and other PPCPs through green and efficient methods from water environments is imminent. As a representative light-Fenton system, photocatalysis has been increasingly implemented in environmental purification territory because it is easy to reach, has no secondary contamination, and exists strong redox ability [6,7]. Basic processes involved in photocatalytic degradation are decomposing PPCPs into small inorganic substances by strong oxidization radical (superoxide radicals (•O$_2^-$), hydroxyl radicals (•OH)) generated in the redox reaction of photocatalyst [5,8,9]. For example, An et al.

previously studied the ability of •OH to effectively degrade persistent contaminants (such as antibiotics) in the aqueous environment into small and non-toxic molecules [10–12]. Therefore, increasing the extent of radicals involved in the photocatalytic reaction system is a promising method to improve degradation efficiency. Many previous efforts are made to enhance the degradation of pollutants by adding extra hydrogen peroxide (H$_2$O$_2$) to provide more hydroxyl radicals [13,14]. Because H$_2$O$_2$ is an eco-friendly oxidant that by-produces are only water and oxygen [8,15] and hydroxyl radicals formed by the decomposition of H$_2$O$_2$ can attack the pollutant non-selectively [15–18]. Usually, in Fenton-like systems, additional Fe(II) ions are needed to realize Fe(III)/Fe(II) cycle reaction to decompose H$_2$O$_2$ into •OH [19,20]. However, the high cost and low efficiency severely limit the efficiency of photocatalysts in degrading pollutants in the presence of H$_2$O$_2$ [21-23]. Therefore, photocatalysts with reducing properties producing innergenerate-H$_2$O$_2$ under simulated solar irradiation for degradation of

pollutants can be an outstanding way. Nevertheless, the yield of H_2O_2 produced under visible light irradiation is relatively low in pure water, due to the huge energy barrier of the hydrogen source in the process of water separate to H_2O_2, thus extra electron donors (ED) (such as iso-propanol (IPA)) can be added to increase the yield [17,24]. Therefore, the innergenerate-H_2O_2 generated under solar irradiation is promising to contribute to the efficient degradation of PPCPs.

Notably, molybdenum disulfide (MoS_2) is an excellent two-dimension (2D) catalyst with two crystalline phase structures with different atomic stacking configurations, 2H-MoS_2 and 1T-MoS_2 of the semiconductor phase and metallic phase, respectively [25–27]. Generally, MoS_2 was previously used mostly as a co-catalyst or substrate [28, 29], but it has the advantage of being a photocatalyst due to its combination of two-phase structures. Among the two phases, 1T-MoS_2 reveals a high photodegradation efficiency than 2H-MoS_2, which is because 1T-MoS_2 exists more catalytically action centers in in-plane and edge [27,30,31]. However, 1T-MoS_2 is metallic and metastable and not naturally formed, and it is easily changeable to 2H-MoS_2 spontaneously [32–34]. Since the conductivity and active sites of 1T-phase are higher than those of 2H-phase, thus, the high content of 1T-phase in mixed-phase MoS_2 may accelerate photogenerated electron transfer, and increase the concentration of electrons [18,35,36]. More importantly, the heterojunction structure at the junction of 2H and 1T-phases not only balances the charge generation and light absorption of 2H-phase, but also facilitates the catalytic reaction at the edge sites of 1T-phase by effective charge separation at the interface [37]. Therefore, the construction of a mixed-phase MoS_2 can improve photocatalytic degradation by increasing the activity of photo-induced carriers while maintaining stability [27,38,39]. In addition, the crucial for increasing ●OH is the presence of the valence-variable metal ion (molybdenum (Mo)) in MoS_2 [19,40]. The presence of valence-variable metal ion and excellent electron transfer capabilities exist in mixed-phase MoS_2 promotes the production of H_2O_2 and the generation of ●OH. For instance, Chen et al. proposed that the accelerated electron transfer due to the heterojunction generated in the 1T and 2H-phases can enhance the production of strong oxidative radicals and thus improve the oxidation capacity [37]. Liu et al. synthesized mixed-phase MoS_2 by the local introduction of 1T-MoS_2 in 2H-MoS_2, which exhibited remarkable hydrogen precipitation reaction properties [41]. Song et al. successfully prepared Au-modified mixed-phase MoS_2 nanosheets for photocatalytic production of H_2O_2 [18]. Moreover, Zhou et al. mentioned that the reducing properties of MoS_2 are beneficial in helping the generation of ●OH [42]. Despite the promise of using 2H/1T MoS_2 in photodegrading pollutants, the issue of limited photo-induced carriers separation and migration, as well as a high photo-induced carriers recombination rate, has been studied comprehensively without being resolved [43]. The most promising solution to the above issue for MoS_2 is defect engineering to enhance more exposed action centers for increasing catalytic performance [44,45]. Luo et al. prepared ultrathin 2D S-defect-rich MoS_2 through the method of ball milling by ascorbic acid, which presented the excellent photocatalytic ability for Cr (VI) [45]. Moreover, Peng and his colleagues significantly improved photocatalytic activity by inducing 1T-MoS_2 transform into 2H-MoS_2 for the introducing S defects on 1T-MoS_2 [46]. However, for mixed-phase MoS_2, studies that produce vacancies at the phase-junction are largely absent.

How can atom vacancies at phase-junction of mixed-phase MoS_2 be prepared simply and conveniently without affecting the photocatalyst structure? The temperature-programmed reduction in hydrogen atmosphere (H_2-TPR) experiment, can be served as a promising approach. According to the previous report, the energy from external thermal field is beneficial to promote different types of vacancies generation for catalysts [47]. In addition, Luo et al. suggested that the modification behavior at the interface junction can effectively enhance the interfacial force to boost photo-induced carriers separation, thus enhancing the photocatalytic performance [48]. Therefore, an external thermal field and hydrogen atmosphere provided by H_2-TPR may offer energy for the

production of in-plane atomic vacancies at phase-junction of mixed-phase MoS_2. The processes associated with the generation of vacancies and defects in catalysts under thermal fields can effectively manipulate photo-induced carriers, thus improving the yield of inner-generate-H_2O_2 and enhancing photocatalytic performance [49].

In our work, we address the challenge of high yields of innergenerate-H_2O_2 to improve degrade PPCPs (e.g., antibiotic contaminants) efficiency in aqueous environments. This is utilizing photocatalysts composed of highly crystalline $Mo_{1-x}S_{2-y}$ nanosheets enriched in S vacancies in the 1T phase at the phase-junction, which is achieved by H_2-TPR experiment. Specifically, the presence of S vacancies in the phase-junction enhances the adsorption of oxygen and promotes the migration and separation of photo-induced carriers, reducing the photo-induced carriers complexation. These all facilitate the generation of ●O_2^-, which effectively produces H_2O_2. And the ●OH generated by H_2O_2 decomposition through the transformation of variable metal Mo atom (Mo(IV)/Mo(VI)) and other radicals (h^+, e^-, ●O_2^-) can effectively degrade pollutants. Therefore, the present work provides a reference for other 2D catalysts for innergenerate-H_2O_2 production and its promotion of pollutant degradation.

2. Experimental section

2.1. Synthesis of bulk MoS_2 and defective MoS_2

A simple one-step hydrothermal method was prepared to synthesize bulk MoS_2 with varying ratios of molybdenum (Mo) and sulfur (S) sources. The specific information is described in the Supporting Information (Part S1.1).

Moreover, the defective MoS_2 was prepared by three different types of preparation methods, i.e. temperature-programmed reduction in hydrogen (H_2-TPR), temperature-programmed desorption of nitrogen (N_2-TPD), and vacuum. The detail processes are given in the Supporting Information (Part S1.2).

2.2. Assessment of photocatalytic activity

Experimental details on all photocatalytic performance, i.e. photo-catalytic degradation of PPCPs experiments, photocatalytic H_2O_2 production experiments, and mechanism correlation experiments are available in the Supporting Information (Part S1.3).

2.3. Characterization and calculation details

Note there exists best degradation performance for DCF solution (Fig. S3) between all defective materials in the orthogonal experiments, thus the subsequent characterization was focused on $Mo_{1-x}S_{2-y}$ (1:9 Mo to S source ratio treated at 310 °C for 2 h after H_2-TPR). Specifically, experiments of characterization and their instruments, as well as information on the methods of the density functional theory (DFT) calculations are listed in the Supporting Information (Part S2).

3. Results and discussion

3.1. Formation of S vacancies at the phase-junction of $Mo_{1-x}S_{2-y}$

Since the temperature-programmed reduction in hydrogen atmosphere (H_2-TPR) is a relationship between the consumption and production rate of the gas and the temperature [50], it can reflect the degree of reaction between the H_2 and the material. Specifically, Fig. 1a presents a plot of the H_2 reduction procedure for MoS_2. There are two temperature regions for the H_2 reduction plot of MoS_2: one is a small peak of a positive signal at low temperatures (100–200 °C) and the other is a more intense absorption peak at 250–360 °C, which is respectively caused by the reversible adsorption of H_2 at low temperatures and the generation of internal sulfur vacancies [51]. Therefore, the above
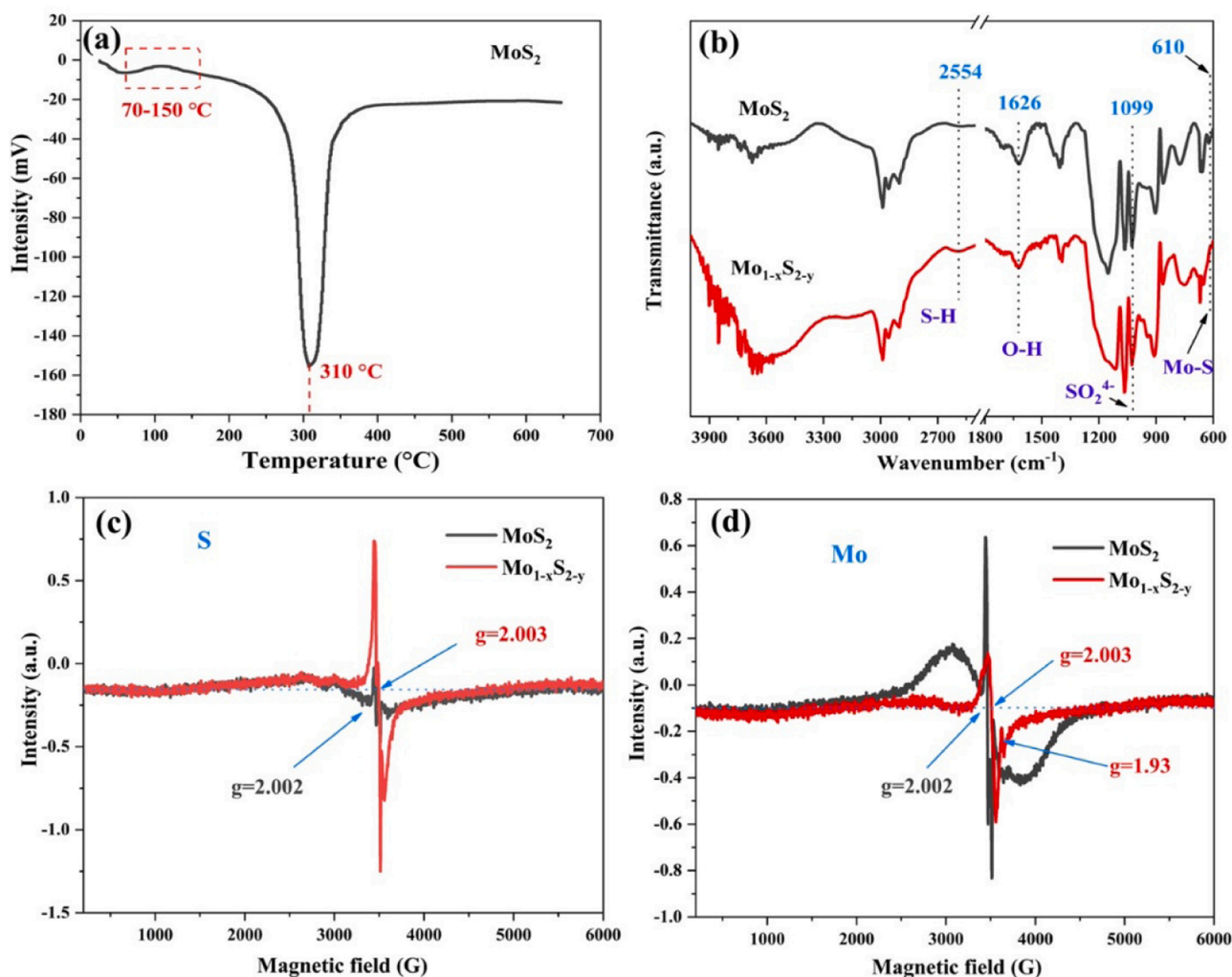
Fig. 1. (a) Experimental TPR spectra for bulk MoS_2. (b) FTIR pattern of MoS_2 and $Mo_{1-x}S_{2-y}$. EPR images of MoS_2 and $Mo_{1-x}S_{2-y}$: (c) S element and (d) Mo element.

analysis indicates that MoS_2 is prone to produce S vacancies in a thermal field under H_2 atmosphere, which may exist excellent photocatalytic properties after modification.

Furthermore, the analysis of the in-plane functional groups of the molecular particles was studied using Fourier-transform infrared spectroscopic detection (FT-IR). Fig. 1b possesses a depressed vibrational peak at 610 cm^{-1} and an enhanced peak at 2554 cm^{-1} after heating treatment at H_2 atmosphere, respectively representing the Mo-S bond and S-H bond [18,52]. This indicates that H_2 combines with the internal S atoms of $Mo_{1-x}S_{2-y}$ during the reaction, leading to the broken of the Mo-S bond and the formation of S vacancies. Moreover, the vibration peak at 1626 cm^{-1} corresponds to a deformation vibration of O-H, which may originate from moisture during material preparation, and the peak at 1099 cm^{-1} can be assigned to the oxidation of the MoS_2 surface leading to the generation of sulfuric acid groups on its surface [53]. In addition, the structure of $Mo_{1-x}S_{2-y}$ does not change significantly, which indicates that the process of H_2-TPR can not destroy the material structure, ensuring the stability of the material.

Therefore, to verify the presence of vacancies in materials, we used a sensitive technique of detecting paramagnetic species i.e. electron paramagnetic resonance (EPR). Fig. 1c exhibits a response signal appearing in g = 2.003 of $Mo_{1-x}S_{2-y}$ (g = 2.002 of MoS_2), revealing the Mo-S dangling bonds and confirming the existence of S vacancies [54]. And the S-vacancy intensity of $Mo_{1-x}S_{2-y}$ is significantly stronger than that of MoS_2, which indicates that $Mo_{1-x}S_{2-y}$ has more S vacancies. In addition, Fig. 1d shows that Mo-S dangling bonds (g = 2.002) are also

present in MoS_2. But for $Mo_{1-x}S_{2-y}$, a signal peak of Mo(III) (g = 1.93) is present in addition to the Mo-S dangling bond [37]. This result suggests that in the thermal field, H_2 reduces MoS_2 to generate Mo(III). Interestingly, MoS_2 exhibits more Mo-S dangling bond, which may be due to the poor crystallinity and the untidy arrangement of atoms after hydrothermal heating. After the H_2-TPR experiment, the structure is aligned neatly, the Mo-S dangling bonds are reduced, which represents the decrease of concentration of Mo vacancies. Since the concentration of Mo vacancy of $Mo_{1-x}S_{2-y}$ is smaller than that of MoS_2, the Mo vacancy is not the main reason for the improved photocatalytic performance. Further, the contents of S, Mo and the atomic percent of C, O, S, and Mo for MoS_2 and $Mo_{1-x}S_{2-y}$ were respectively detected by inductively coupled plasma-optical emission spectrometry (ICP-OES) and X-ray photoelectron spectroscopy (XPS) (Table 1). The results of XPS

Table 1
ICP-OES test results and element analysis (obtained by XPS) of C, O, S, and Mo atomic percent for MoS_2 and $Mo_{1-x}S_{2-y}$.

Materials	Elements analysis obtained by XPS				ICP-OES test results	
	C (Atomic %)	O (Atomic %)	S (Atomic %)	Mo (Atomic %)	S (wt %)	Mo (wt%)
MoS_2	5.59	23.39	19.85	51.16	26.23	31.95
$Mo_{1-x}S_{2-y}$	4.63	20.92	13.61	60.53	20.37	18.03

and ICP-OES suggest that the weight ratio of S atoms and their atomic ratio have decreased, indicating the presence of S vacancies. An increase in the atomic ratio of Mo and a decrease in the weight ratio of Mo may be owing to the different presence forms of Mo atoms. The C and O atoms probably originate from the adsorbed magazines and water on the surface. Therefore, the above analysis indicates that MoS_2 is prone to produce S vacancies through the Mo-S bond being broken during the H_2-TPR experimental process.

We have demonstrated that H_2-TPR can effectively generate S vacancies in $Mo_{1-x}S_{2-y}$, and to further investigate the location of the presence of S vacancies, we investigated the internal crystalline phase structure of the material. To obtain the variation in the morphology of the products after the formation of S vacancies, scanning electron microscopy (SEM) images of MoS_2 and $Mo_{1-x}S_{2-y}$ are provided in Fig. 2a, b and Fig. S7, where show the presence of classical MoS_2 nanoflower microspheres despite the large difference in morphology. This indicates that the basic structure of $Mo_{1-x}S_{2-y}$ is not damaged when forming S vacancies under the action of an external thermal field in the H_2 atmosphere. Remarkably, the diameter of $Mo_{1-x}S_{2-y}$ (around 0.2 μm) microspheres is significantly smaller than that of MoS_2 (about 1 μm) microspheres. In addition, combined with the transmission electron microscopy (TEM) images of the materials (Fig. S8), it can be visualized that the lamellar structure of nanosheets is smaller and more crimped because the breakage of the Mo-S bonds around the S vacancies produce dangling bond that causes the atoms to deviate from their normal position, resulting in a curled morphology [55]. This contributes to the enhanced active sites of material and the reaction area in contact with the contaminants, thus improving the photodegradation efficiency.

Combining the high-resolution transmission electron microscopy (HRTEM) images of the materials (Fig. 2c and d), it can be visualized that the atoms are significantly shaken, the 1T-phase structure is increased and the crystallinity of the material is improved after the H_2-TPR experiments. Specifically, the HRTEM image of MoS_2 (Fig. 2c) shows the typical 2H-phase nanosheets with an interlayer spacing of 6.2 Å [53,56]. Surprisingly, through H_2-TPR treatment, $Mo_{1-x}S_{2-y}$ presents a neat lattice structure arrangement compared to MoS_2, with an extra lattice spacing of 2.7 Å in the basal plane, which is in good accordance with the (101) planes of 2H-phase [56]. At the same time, a small portion of the phase structure corresponding to the 1T-phase with a lattice spacing of 3.2 Å (004) can also be observed [57]. Thus, the above analysis proves that H_2-TPR experiments neatly align the atoms in the phase structure through atomic vibrations, thus improving the orderliness, increasing the 1T-phase content, and enhancing the crystallinity of the phase structure.

X-ray diffraction (XRD) patterns (Fig. 2e) can be seen that MoS_2 exists only one distinct diffraction peak belonging to the (002) lattice plane at $2\theta = 14.4°$ [58]. As a comparison, $Mo_{1-x}S_{2-y}$ shows significantly stronger peaks than MoS_2 for (002) ($2\theta = 14.4°$), (101) ($2\theta = 33.5°$), (103) ($2\theta = 33.5°$), and (110) ($2\theta = 58.3°$) planes (JCPDS 37–1492) [56,59], which indicates the enhanced crystallinity of $Mo_{1-x}S_{2-y}$. The generation of S vacancies can result in an inhomogeneous charge distribution at the interface, leading to the presence of alternating inhomogeneous layers of charge in the layered structure of $Mo_{1-x}S_{2-y}$, and therefore the establishment of an interlayer electric field

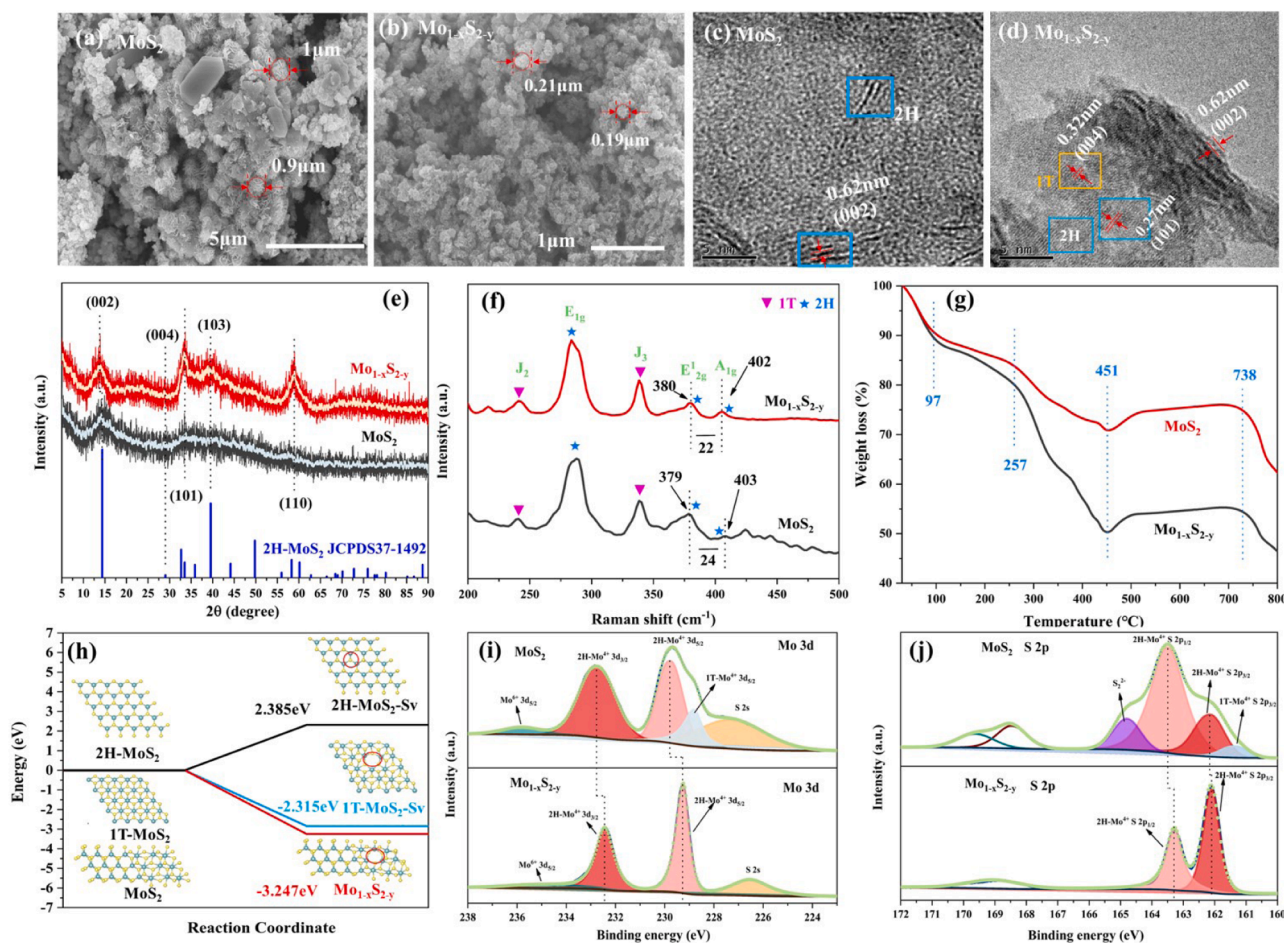**Fig. 2.** SEM images of (a) MoS_2 and (b) $Mo_{1-x}S_{2-y}$. HRTEM images of (c) MoS_2 and (d) $Mo_{1-x}S_{2-y}$. (e) XRD, (f) Raman and (g) TGA patterns of MoS_2 and $Mo_{1-x}S_{2-y}$. (h) Graph of S vacancies formation energy of 2H-MoS_2, 1T-MoS_2, MoS_2 and $Mo_{1-x}S_{2-y}$, the yellow and blue spheres refer to S and Mo atoms, respectively. (i) XPS Mo 3d and (j) XPS S 2p images of MoS_2 and $Mo_{1-x}S_{2-y}$.

[60]. Moreover, the (002) peak position of $Mo_{1-x}S_{2-y}$ is shifted left by 0.17° compared to that of MoS_2, indicating an increase in the interlayer distance due to the creation of S vacancies [61,62], which can facilitate the electron transport. More importantly, for $Mo_{1-x}S_{2-y}$, a smaller peak appears at $2\theta = 29.0°$ (004), which represents the $1T-MoS_2$ pattern. This suggests that $Mo_{1-x}S_{2-y}$ is mixed-phase material (i.e., it possesses both 1T and 2H-phase structures) and the content of 1T-phase is increased caused by atomic vibrations and rearrangements. The 2H phase has active sites only at the edge positions, while the 1T-phase has active sites at both surface and edge positions [27], thus the high content of 1T-phase is beneficial to the increase of reaction sites, which improves the photocatalytic performance.

To further understand the phase structure composition of the photocatalysts after the experiments of H_2-TPR, we took the Raman experiment. In the Raman spectrum (Fig. 2f), all characteristic peaks of MoS_2 and $Mo_{1-x}S_{2-y}$ at 283, 379, 403 cm^{-1} originate from E_{1g}, E^1_{2g}, A_{1g}, which are all characteristic peaks of the 2H-phase. Another, two representative peaks located at 219 cm^{-1} and 335 cm^{-1} can vest in the 1T-phase [63]. This result indicates that both MoS_2 and $Mo_{1-x}S_{2-y}$ belong to the mixed-phase catalysts. Interestingly, the 1T-phase content increases slightly after H_2-TPR process, which reflects the high contents of 1T for $Mo_{1-x}S_{2-y}$. In addition, the E^1_{2g} and A_{1g} modes respectively represent the in-plane vibration of S atoms and the symmetric displacement outside the layer of Mo-S bond [45,64]. The E^1_{2g} peak vibrations of $Mo_{1-x}S_{2-y}$ are weakened and A_{1g} peak vibrations of $Mo_{1-x}S_{2-y}$ are enhanced, respectively indicating the significant presence of vacancies and strength of interlayer force, which reflects vibrational and rearrangement activities of Mo and S atoms within the layer [45,65]. Furthermore, the frequency difference between the Raman peaks of MoS_2 ($\Delta = A_{1g}-E^1_{2g}$) is estimated to be 24 cm^{-1}, and the spacing of the peaks of $Mo_{1-x}S_{2-y}$ decreases (22 cm^{-1}) after H_2 reduction, indicating a decrease of the number of layers of $Mo_{1-x}S_{2-y}$ [63]. This is consistent with the XRD analysis above, where the reduction leads to an increase in the lamellae spacing, which facilitates electron transport and thus improves photocatalytic performance.

Thermogravimetric (TGA) was observed under a nitrogen atmosphere to understand the thermal stability of MoS_2 and $Mo_{1-x}S_{2-y}$ (Fig. 2g). $Mo_{1-x}S_{2-y}$ exhibits a significantly stronger thermal stability, owing to S vacancies. Furthermore, MoS_2 and $Mo_{1-x}S_{2-y}$ show mass loss at 257 °C, representing a phase change in the lamellae [59]. This result suggests that the additional thermal field favors atomic vibrations, leading to phase vibrations and thus phase transitions. And the phase change can promote the production of S vacancies during the thermal reduction process, thus improving the thermal stability. In addition, there is an upward weight increase peak from 450 °C to 750 °C, probably due to the adsorption of nitrogen during the process.

Therefore, to clarify the location of S vacancies within the material and gain a comprehensive understanding of the formation of S vacancies in materials from atomic and energetic angles, we have further calculated the S vacancy formation energy of catalysts using first-principles DFT calculations. In our calculation, $2H-MoS_2$, $1T-MoS_2$, MoS_2 and $Mo_{1-x}S_{2-y}$ were modeled (Mo and S indicated as blue and yellow spheres). And the formation energy (E_f) has been calculated as follows (Eq. (1)):

$$E_f = E_{S\ vacancy} + \left(E_{H2S\ (g)} - E_{H2\ (g)}\right) - E_{total} \tag{1}$$

where $E_{S\ vacancy}$ and E_{total} respectively represent the energy with and without the vacancy of S atoms. And the $E_{H2S\ (g)}$ and $E_{H2\ (g)}$ are the energy of H_2S (g) and H_2 (g). Fig. 2h shows that the formation energy of S vacancy in $1T-MoS_2$ is a negative value (−2.315 eV), which is lower than that of $2H-MoS_2$ (2.385 eV), indicating that $1T-MoS_2$ is more spontaneously prone to S vacancies formation [66]. Most importantly, the interfacial structure formed by the 2H and 1T-phases plays a crucial role in the determination of S vacancies. There are two junction ways for the interface between the 2H and 1T-phases, one dominated by S atom

(S of 2H connect with Mo of 1T) and the other dominated by Mo atom (Mo of 2H connect with S of 1T). The distinct bonding structures at the interface junctions lead to different kink formation energies. Zou et al. verify that of the following two connections, Mo-dominated interfaces with low kink formation energies and low activation potentials while S-dominated interfaces that are more stable because of their higher kink formation energies, that means the former connection has significantly unstable, which determines their dominance in the generation S vacancies [67]. It is well known that the lower the potential barrier, the easier the process is to proceed. Therefore, $Mo_{1-x}S_{2-y}$ is most likely to exhibit S vacancies in 1T-phase at the phase-junction dominated by Mo atoms. It can be seen from Fig. 2h that the formation energy of S vacancies of $Mo_{1-x}S_{2-y}$ is equal to − 3.247 eV, which is more negative than formation energies of S vacancies in pure phase, indicating a more spontaneous formation of S vacancies in 1T-phase at the phase-junction [68]. Therefore, based above discussion, it suggests H_2 are most likely to break the Mo-S bond dominated by Mo atoms in the 2H-phase at the junction in $Mo_{1-x}S_{2-y}$ during H_2-TPR process, as a result, S vacancies are mainly produced in 1T-phase of the phase-junction.

Moreover, the XPS spectra of MoS_2 and $Mo_{1-x}S_{2-y}$ (Fig. 2h and i) are further analyzed in detail. The binding energy (BE) peaks at 229.8, 232.8, 163.6, and 162.2 eV in the Mo 3d and S 2p spectra of MoS_2 are respectively consistent with Mo (IV) $3d_{3/2}$, Mo (IV) $3d_{5/2}$, Mo (IV) $2p_{1/2}$ and Mo (IV) 2p $_{3/2}$ of $2H-MoS_2$, while the resonances of 228.5 and 161.4 eV respectively correspond to Mo (IV) $3d_{5/2}$ and Mo (IV) $2p_{3/2}$ of $1T-MoS_2$ [59,69]. And for $Mo_{1-x}S_{2-y}$, in Mo 3d and S 2p spectra, the BE of the 2H-phase moves to a lower level, which indicates that the e^- of Mo and S atoms in 2H-phase transfer to the 1T-phase [70]. This result laterally confirms the S vacancies in the 1T-phase. Another, the Mo^{6+} $3d_{5/2}$ peak appears in the MoS_2 and $Mo_{1-x}S_{2-y}$ spectra, but the intensity of the Mo^{6+} $3d_{5/2}$ peak decreases after H_2 reduction, indicating that MoS_2 is partially reduced by oxidized Mo atoms [59]. In addition, the disappearance of the 1T-phase in $Mo_{1-x}S_{2-y}$ may be due to the electrons leaving the d/p orbitals during the partial phase transition in H_2-TPR experiment [69]. Therefore, the above analysis shows that after the H_2-TPR experiment, the atomic vibrations rearrange, the crystallinity of $Mo_{1-x}S_{2-y}$ increases, and the content of the 1T-phase is improved. This facilitates the increase of S vacancies in the 1T-phase at the phase-junction, which provides more active sites for the degradation of pollutants.

3.2. High innergenerate-H_2O_2 synergistic enhance photodegradation efficiency

An in-depth understanding of improving photocatalytic performance by the formation of S vacancies in the 1T-phase from an atomic and energetic perspective is essential. As is well-known, the lower the free energy of adsorption ($|\Delta G_H|$) of H, the higher the catalytic activity [71]. Hence, to reveal the excellent photocatalytic performance of $Mo_{1-x}S_{2-y}$, we evaluated the $|\Delta G_H|$ on materials using first-principles DFT calculations. The models for H_2 adsorption on mixed-phase MoS_2, mixed-phase $Mo_{1-x}S_{2-y}$, $1T-MoS_2$, and $2H-MoS_2$ are depicted in Fig. 3a, respectively. Where $2H-MoS_2$ has an extremely high $|\Delta G_H|$ value of 2.39 eV and the $|\Delta G_H|$ of $1T-MoS_2$ is 1.51 eV, they are all larger than mixed-phase MoS_2 (0.74 eV). This intuitively indicates that the mixed-phase MoS_2 possesses high photocatalytic efficiency than $2H-MoS_2/1T-MoS_2$. When introducing S vacancies in 1T-phase at the phase-junction, the $|\Delta G_H|$ of $Mo_{1-x}S_{2-y}$ is equal to − 0.64 eV, and the absolute value is closer to 0 eV. This analysis indicates that S vacancies can effectively improve the photocatalytic performance of the catalyst.

Photocatalytic degradation of PPCPs such as antibiotics has attracted widespread attention due to its persistence and recalcitrance. To investigate the degradation performance of MoS_2 and $Mo_{1-x}S_{2-y}$ for PPCPs, the degradation of DCF, TC, and mixed-phase antibiotics solution (contains 5 ppm of TC, 5 ppm of SMZ, and 5 ppm of CHL) under simulated solar irradiation is performed. It is obvious from Fig. 3b, c, S9, and
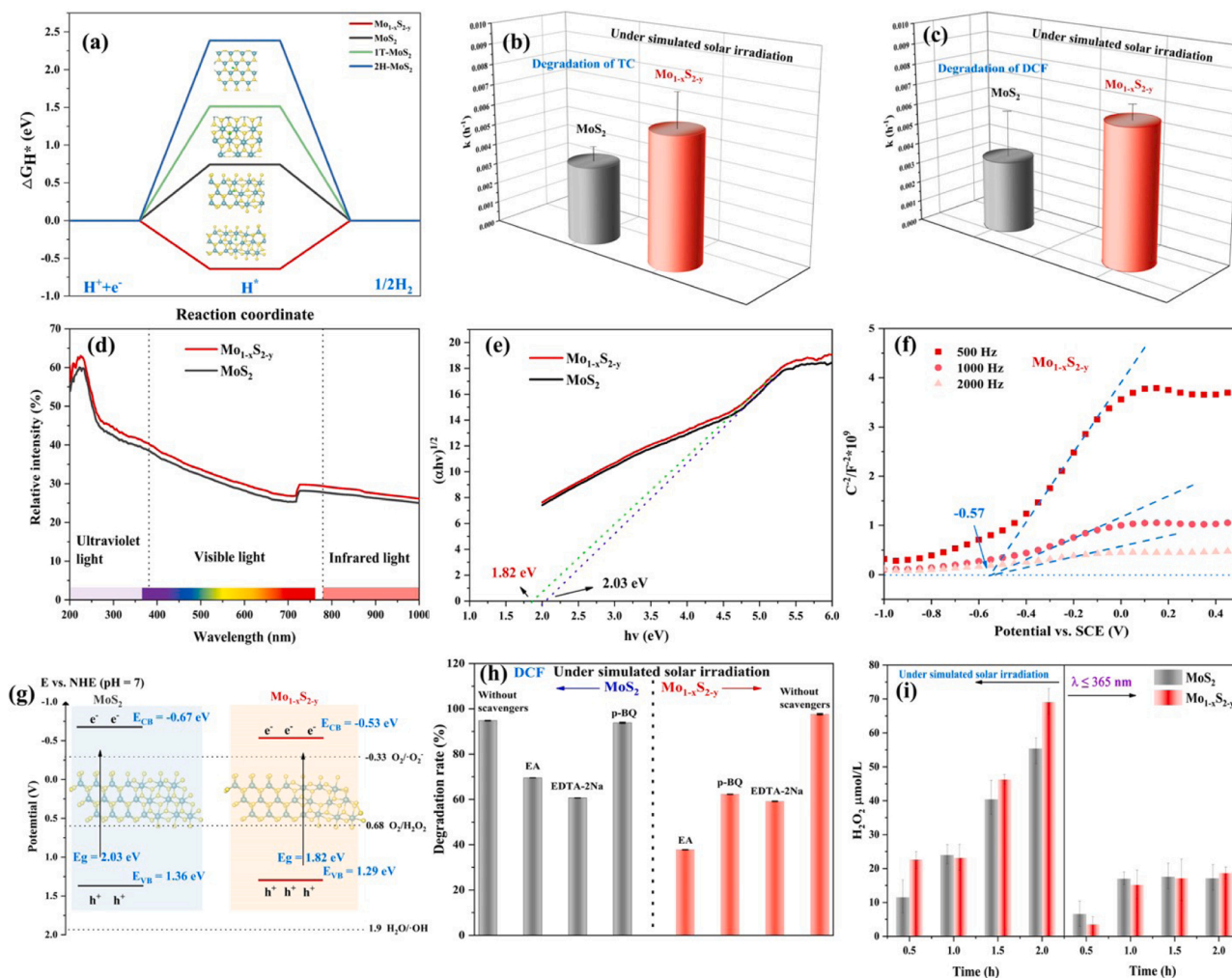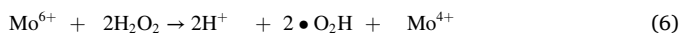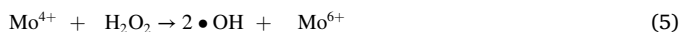
Fig. 3. (a) Gibbs free energy of MoS_2, $Mo_{1-x}S_{2-y}$, 1T-MoS_2, and 2H-MoS_2 used in DFT calculations. Where the green, yellow, and blue spheres respectively refer to H, S, and Mo atoms. (b, c) Degradation efficiencies of MoS_2 and $Mo_{1-x}S_{2-y}$ for TC and DCF under simulated solar irradiation. (d) UV–vis DRS absorption spectra, and (e) corresponding energy gap of MoS_2 and $Mo_{1-x}S_{2-y}$. (f) Mott-Schottky curves of $Mo_{1-x}S_{2-y}$. (g) The bandgap schematic representation of MoS_2 and $Mo_{1-x}S_{2-y}$. (h) Quenching experiments of reactive radicals generated by MoS_2 and $Mo_{1-x}S_{2-y}$ catalysts during the degradation of MB solutions. (i) The yield of H_2O_2 produced by the MoS_2 and $Mo_{1-x}S_{2-y}$ catalysts under simulated solar irradiation and UV irradiation ($\lambda \leq 365$ nm), respectively.

S10 that $Mo_{1-x}S_{2-y}$ possesses excellent efficiency in degrading the DCF and TC, and the degradation efficiency after 120 min is basically nearly twice as high as that of MoS_2. This indicates that the S vacancies in 1T-phase of the phase-junction contribute to degrading pollutants. In addition, the low degradation rate for SMZ and CHL (Fig. S9) is due to the selectivity of the material. The light absorption properties are important for photodegradation, so the UV-Vis diffuse reflectance spectra (DRS) were investigated. As shown in Fig. 3d, the light absorption curves of MoS_2 and $Mo_{1-x}S_{2-y}$ are essentially the same, with the intrinsic absorption edge of $Mo_{1-x}S_{2-y}$ shifted slightly to the right, indicating that the light utilization of $Mo_{1-x}S_{2-y}$ for the visible region is higher than that of the MoS_2 [72]. The corresponding band gaps for MoS_2 and $Mo_{1-x}S_{2-y}$ were also also estimated to be 2.03 and 1.82 eV (Fig. 3e). The results suggest that the S vacancies facilitate the narrowing of the bandwidth and enhance the electron transfer, thus improving the photodegradation efficiency. To determine the positions of the conduction and valence bands (CB, VB) of MoS_2 and $Mo_{1-x}S_{2-y}$, Mott-Schottky measurements were performed. As shown in Fig. 3f and S11, the calculated flat-band potentials (E_{fb}) for MoS_2 and $Mo_{1-x}S_{2-y}$ are − 0.71 and − 0.57 eV, respectively. Therefore, through calculation, the CB of MoS_2 and $Mo_{1-x}S_{2-y}$ respectively are − 0.67 and − 0.53 V (vs. NHE, pH = 7) [73]. From the bandgap schematic representation (Fig. 3g), it is obvious that electrons are more likely to leap for

$Mo_{1-x}S_{2-y}$, thus enhancing the increase in active species and enhancing photodegradation efficiency.

The photodegradation is due to the oxidation of pollutants by a large number of reactive species such as hole (h^+), hydroxyl radical ($^\bullet OH$), and superoxide radical ($^\bullet O_2^-$) produced in the catalyst. More importantly, $^\bullet OH$ is the most powerful oxidant in water treatment, (E = 1.9–2.7 V), due to its non-selective aggressiveness and high diffusion rate (10^{10} m^{-1} s^{-1}) [16]. However, it can be seen by Fig. 3g that none of the VBs of MoS_2 and $Mo_{1-x}S_{2-y}$ satisfy a high oxidation potential of 1.9 V to generate $^\bullet OH$. To understand the species of active species in the system, we use three scavengers, EDTA-2Na, EA, and p-benzoquinone, to detect different active species (h^+, $^\bullet OH$, $^\bullet O_2^-$) in MoS_2 and $Mo_{1-x}S_{2-y}$ degraded MB solutions, respectively. As can be seen from Fig. 3i, for $Mo_{1-x}S_{2-y}$, the photodegradation rates of MB solutions are reduced to different degrees after the addition of the three scavengers, which reveals that the active species of h^+, $^\bullet OH$, and $^\bullet O_2^-$ all exists. While MoS_2 has only two active species (h^+ and $^\bullet OH$). Therefore, in combination with the energy band gap position, the $^\bullet OH$ in the system basically comes from the decomposition of innergenerate-H_2O_2. According to the principle of H_2O_2 production reaction and the differences in the active species produced, Lou et al. suggested that the innergenerate-H_2O_2 from photocatalysts can be induced by five different pathways [17]. Therefore, in combination with the active substance of

MoS$_2$ and Mo$_{1-x}$S$_{2-y}$ and previous reports [17], the main pathway for the production of innergenerate-H$_2$O$_2$ is as follows:

$$Photocatalysts + hv \rightarrow e^- + h^+ \tag{2}$$

$$e^- + O_2 \rightarrow \bullet O_2^- \tag{3}$$

$$\bullet O_2^- + e^- + 2H^+ \rightarrow H_2O_2 \tag{4}$$

$$Mo^{4+} + H_2O_2 \rightarrow 2\bullet OH + Mo^{6+} \tag{5}$$

$$Mo^{6+} + 2H_2O_2 \rightarrow 2H^+ + 2\bullet O_2H + Mo^{4+} \tag{6}$$

Specifically, under simulated solar irradiation, the unpaired e$^-$ are activated to migrate and form h$^+$ (Eq. (2)). The exciting e$^-$ is transferred to catalysts surface and combine with adsorbed O$_2$ to form $\bullet$O$_2^-$ (Eq. (3)). Then e$^-$ further reduces $\bullet$O$_2^-$ to O$_2^{2-}$, and the proton (H$^+$) in reaction system combines with O$_2^{2-}$ to form HO$_2^-$ and finally the HO$_2^-$ gradually approaches the H$^+$ to form H$_2$O$_2$ (Eq. (4)). Finally, the reaction of valence-variable metal ion (Mo(IV)/Mo(VI)) facilitates H$_2$O$_2$ the decomposed to $\bullet$OH and the production of more H$_2$O$_2$ (Eq. (5) and Eq. (6)) [19,40].

Therefore, the H$_2$O$_2$ production experiments were conducted to investigate the innergenerate-H$_2$O$_2$ yield of MoS$_2$ and Mo$_{1-x}$S$_{2-y}$. The experiment result (Fig. S12) shows that the innergenerate-H$_2$O$_2$ yield of Mo$_{1-x}$S$_{2-y}$ was higher than that of MoS$_2$ in pure water under simulated solar irradiation, which indicates that the S vacancy can effectively increase the yield of innergenerate-H$_2$O$_2$. However, because of the huge energy barrier of the H$^+$ source in the process of water separation, resulting in a low yield of innergenerate-H$_2$O$_2$. Therefore, extra electron donors (ED) (i.e. isopropanol (IPA)) were added to increase the yield [24,48]. The experiment shows that the yield of H$_2$O$_2$ with IPA (Fig. 3h) was 4.2 times higher than that without IPA under simulated solar irradiation, and the yield of H$_2$O$_2$ produced by Mo$_{1-x}$S$_{2-y}$ under simulated solar irradiation is higher than that of MoS$_2$ in 2h. This result indicates that the S vacancy is favorable to increase the yield of H$_2$O$_2$ under the condition of abundant H$^+$ source. The dangling bonds created by S vacancies can deflect surface atoms from their normal position and affect several layers around the bonds, causing the lamellae of Mo$_{1-x}$S$_{2-y}$ to curl and thus improve adsorb of oxygen [55,74]. In addition, the higher energy around the dangling bond provides more active sites for the production of H$_2$O$_2$ [55,74]. These are conducive to increasing the number of $\bullet$O$_2^-$ in Mo$_{1-x}$S$_{2-y}$ and thus improve the yield of H$_2$O$_2$. In the radical quenching experiment, Mo$_{1-x}$S$_{2-y}$ exhibits $\bullet$O$_2^-$, while basically no $\bullet$O$_2^-$ is detected in MoS$_2$. This may be since some of the $\bullet$O$_2^-$ are still able to be used for contaminant degradation after the production of H$_2$O$_2$, and thus the contaminant degradation efficiency of Mo$_{1-x}$S$_{2-y}$ is increased. Moreover, MoS$_2$ and Mo$_{1-x}$S$_{2-y}$ can produce H$_2$O$_2$ under simulated solar and UV light with isopropyl alcohol (IPA) (Fig. 3h), but the yield of H$_2$O$_2$ under simulated solar is higher than that under UV light. This result indicates that although MoS$_2$ and Mo$_{1-x}$S$_{2-y}$ show a wide range of light response degrees, it is more utilized for the white light portion. Furthermore, the yield of Mo$_{1-x}$S$_{2-y}$ under simulated solar light is higher than that of MoS$_2$, while the yield under UV light is similar, which indicates that the Mo$_{1-x}$S$_{2-y}$ are more favorable to excite electron migration under simulated solar irradiation, thus improving the photocatalytic activity.

Usually, some Fenton systems are used to achieve efficient pollutant degradation by adding additional H$_2$O$_2$. We further investigated the degradation performance of DCF by adding H$_2$O$_2$. From Figs. S13a and S10b, for Mo$_{1-x}$S$_{2-y}$, the degradation rate of DCF without H$_2$O$_2$ is nearly 100% (Fig. S10b), which is higher than that with H$_2$O$_2$ (10%) (Fig. S13a). And for MoS$_2$, the effect of adding H$_2$O$_2$ in degrading DCF was not obvious, and the degradation rate was about 40%. The poor degradation rate may owe to H$_2$O$_2$ being an electron trapping agent [75]. When a large amount of H$_2$O$_2$ is added, e$^-$ excited by S vacancies in Mo$_{1-x}$S$_{2-y}$ react with H$_2$O$_2$, resulting in the adding H$_2$O$_2$ inefficiently

being decomposed into $\bullet$OH to oxidize the contaminants. In addition, the trapped e$^-$ cannot combine with O$_2$ to generate $\bullet$O$_2^-$, therefore, the addition of H$_2$O$_2$ leads to low photodegradation efficiency.

In addition, we also explored the stability of the materials. As can be seen from Fig. S14a, the innergenerate-H$_2$O$_2$ yields of MoS$_2$ and Mo$_{1-x}$S$_{2-y}$ decreased from the second round in the cyclic experiment (2 h per round). The activity of S ion-based semiconductor photocatalysts is strongly influenced by photocorrosion. These catalysts produce photo-induced carriers that react with the O^{2-} or S^{2-} portion of the catalysts, resulting in a change in catalysts composition and a reduction in photocatalytic performance [76]. Therefore, in our system, materials are photocorroded and have a lower performance in cyclic H$_2$O$_2$ production without sacrificial agents. However, in the fourth round, the innergenerate-H$_2$O$_2$ yields of Mo$_{1-x}$S$_{2-y}$ are still up to 10 μmol L^{-1} h^{-1}, which is 5 times as high as bulk MoS$_2$ (2 μmol L^{-1} h^{-1}). Thus, Mo$_{1-x}$S$_{2-y}$ has a relatively excellent photocatalytic stability. Remarkably, ICP-OES were tested by different instruments before and after the cyclic experiment, thus their values are very different, but the ratio of S/Mo is essentially the same. Therefore, in Fig. S14b, the results of inductively coupled plasma mass spectrometry (ICP-MS) and ICP-OES experiments confirm that the values of MO and S elements and their ratios were essentially unchanged after cycling experiments. Furthermore, it can be seen in FTIR patterns (Fig. S14c and d) that the structure of Mo$_{1-x}$S$_{2-y}$ basically remains after the cycling experiments. However, for MoS$_2$, peaks of 3280 and 2554 cm^{-1} respectively corresponded to OH$^-$ and H-S [77]. This indicates that the structure of MoS$_2$ was slightly destroyed after the cycling experiment. Therefore, after H$_2$-TPR treatment, S vacancies improve the crystallinity of Mo$_{1-x}$S$_{2-y}$, leading to the enhanced stability. In addition, the results of XPS (Fig. S14e and f) after cycling show that catalysts maintain the basic phase structure compared to the pre-cycling period (Fig. 2i and j). Moreover, it can be seen from the graphs of morphology and element distribution (Fig. S15) that the morphology of the catalysts is unchanged after the cyclic experiment. Therefore, after four rounds of cyclic experiments of producing innergenerate-H$_2$O$_2$, H$_2$O$_2$ could still be produced. Therefore, the S vacancy facilitates the stability of Mo$_{1-x}$S$_{2-y}$ by increasing the crystallinity.

Thus, in summary, the specific process of high production yield of innergenerate-H$_2$O$_2$ to promote pollutant degradation can be described as follows. The creation of S vacancies leads to the presence of dangling bonds that promote the curling of the lamellae, thus enhancing the adsorption for O$_2$. The unsaturated e$^-$ generated by S vacancies on the lamellae of Mo$_{1-x}$S$_{2-y}$ migrate rapidly under the excitation of simulated solar light irradiation. In addition, the e$^-$ is transferred to the material surface so that the $\bullet$O$_2^-$ is further reduced and then combined with H$^+$ in the system to increase the yield of H$_2$O$_2$. The innergenerate-H$_2$O$_2$ then combines with Mo(IV) in the Mo$_{1-x}$S$_{2-y}$ to promote the production of $\bullet$OH. The $\bullet$OH and surplus $\bullet$O$_2^-$ attacks the contaminant. Therefore, the processes of producing high yield innergenerate-H$_2$O$_2$ can improve degrade pollutants efficiency.

3.3. Behavior of charge produced by S vacancies

From the above study, we believe that in the structure of mixed-phase Mo$_{1-x}$S$_{2-y}$, the H$_2$ breaks the Mo-S bond at the phase-junction during the reduction process, resulting in the S vacancies in the 1T phase of the phase-junction. Thus, the presence of lone pair electrons at Mo atoms promotes the enhancement of photo-induced carriers, which can significantly enhance the separation and migration rate of photo-induced carriers. To verify the electron migration process of the material, differential charge density is investigated using theoretical calculations. In our calculation, MoS$_2$ and Mo$_{1-x}$S$_{2-y}$ samples were modeled. The top and side views of MoS$_2$ and Mo$_{1-x}$S$_{2-y}$ are shown in Fig. S15 (Mo and S indicated as blue and yellow spheres). As can be seen in Fig. 4a-d, the S vacancies lead to a large number of electrons enriched around the Mo atom in 1T phase. This result indicates that the S vacancies help to enhance the electron transfer, which can effectively
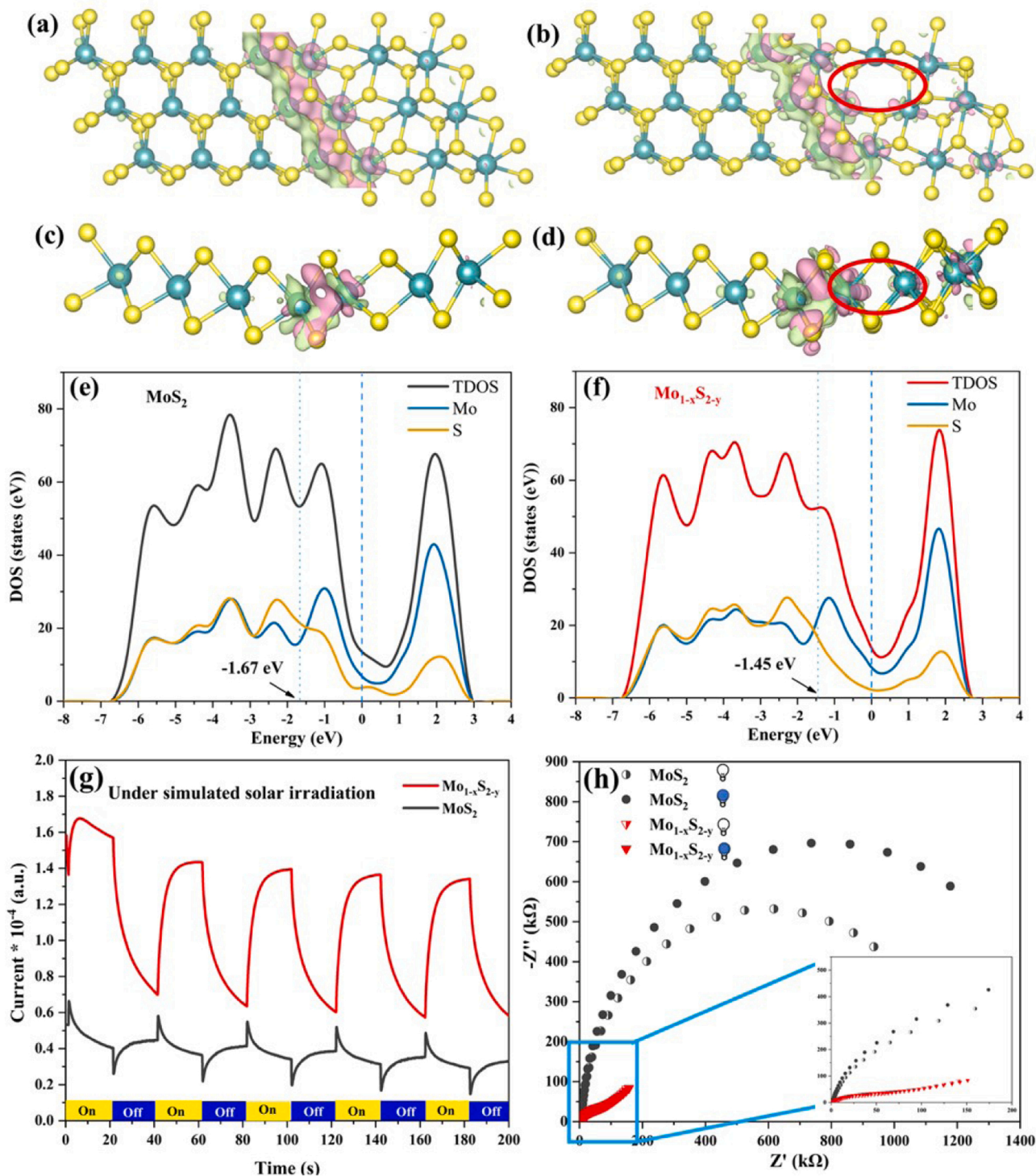
Fig. 4. Differential charge density diagram of (a, c) MoS_2 and (b, d) $Mo_{1-x}S_{2-y}$. Where the pink area indicates electron enrichment and the light green area indicates electron loss. Top view of (a) MoS_2 and (b) $Mo_{1-x}S_{2-y}$. Side view of (c) MoS_2 and (d) $Mo_{1-x}S_{2-y}$. DOSs for (e) MoS_2 and (f) $Mo_{1-x}S_{2-y}$. (g) Photocurrent spectra and (h) EIS Nyquist plots of MoS_2 and $Mo_{1-x}S_{2-y}$.

improve the degradation rate. Furthermore, the density of states (DOS) of materials is studied for electronic properties. Fig. 4e and f show the result that the total densities of states (TDOS) intensities of MoS_2 and $Mo_{1-x}S_{2-y}$ at the Fermi level are not equal to zero indicating the metallic character of 1T phase [78]. In addition, the S element DOS intensity of $Mo_{1-x}S_{2-y}$ (Fig. 4f) near the Fermi energy level strengthen after S vacancy generation compared to MoS_2 (Fig. 4e), which because of the modification of the electronic structure of $Mo_{1-x}S_{2-y}$ by the S vacancies

generation, indicating that $Mo_{1-x}S_{2-y}$ exists a stronger electron-donating ability [79]. Photocurrent, photoluminescence (PL), and electrochemical impedance spectroscopy (EIS) are all studied to investigate the behavior of photoelectrons in MoS_2 and $Mo_{1-x}S_{2-y}$. The photocurrent intensity (Fig. 4g) of $Mo_{1-x}S_{2-y}$ is stronger than that of MoS_2 when the light is on. This conclusion implies that the generation of S vacancies in the 1T phase can effectively improve the photo-induced carrier transfer efficiency within $Mo_{1-x}S_{2-y}$, resulting in a better

$Mo_{1-x}S_{2-y}$ photoresponse [80]. It is noteworthy that the photocurrent signals are still present in MoS_2 and $Mo_{1-x}S_{2-y}$ when it is dark, which may be due to the high conductivity of the metallic nature of the 1T phase [81]. In addition, Fig. S17 shows a significant fluorescence burst behavior in all samples, which because of the radiative complexation of photo-induced carrier. However, it is noteworthy that $Mo_{1-x}S_{2-y}$ has a weaker emission peak compared to MoS_2. This can be attributed to the suppressed compounding rate and improves the separation efficiency of the photo-induced carriers of $Mo_{1-x}S_{2-y}$ [82]. The smaller arc radius in electrochemical impedance spectra (EIS) Nyquist curves of the samples, the smaller charge migration resistance, and higher separation efficiency. The arc radius of $Mo_{1-x}S_{2-y}$ (Fig. 4h) is significantly smaller than that of MoS_2 in the on-lamp and off-lamp states, indicating that S vacancy in 1T phase can prove the separation rate of photo-induced carriers and thus their photocatalytic activity [83]. The above results demonstrate that the broken Mo-S bond creates high S vacancies in the 1T phase at the phase-junction, which can promote the non-uniform electron distribution. This benefits to the generation of electric fields in the vertical direction, increasing the crystallinity of the material. These all can improve the photo-induced carrier migration and separation efficiency and enhance the photoresponse, thus significantly improving the photocatalytic performance.

To verify whether the adsorption of $Mo_{1-x}S_{2-y}$ is responsible for the enhanced photocatalytic performance, the BET surface area and porosity were evaluated using N_2 adsorption-desorption isotherms. Fig. S18 respectively shows the BJH pore size distribution and the N_2 adsorption-desorption measurements of MoS_2 and $Mo_{1-x}S_{2-y}$, where exhibit a hysteresis type IV of isotherms for samples [84]. The BJH plots show that the pore sizes of MoS_2 and $Mo_{1-x}S_{2-y}$ are mainly distributed in the range

of 2–50 nm, indicating that the material is mainly mesoporous with only a few macroporous pores [85]. The surface area and average pore sizes of samples are listed in Table S4. The specific surface area of the $Mo_{1-x}S_{2-y}$ sample is 30.5993 $cm^2\ g^{-1}$, which is smaller than that of $Mo_{1-x}S_{2-y}$ (62.5838 $cm^2\ g^{-1}$). This result may be because stacked pores built up between the large lamellae of MoS_2 facilitate the entry of nitrogen and the complete adsorption-desorption process, thus leading to the increase of surface area. While after reduction by H_2, the nanosheets of $Mo_{1-x}S_{2-y}$ is very small, the stacking pore structure is very tiny and nitrogen cannot enter, resulting in a smaller BET surface area. Therefore, the specific BET surface area of this system is not the main reason for the high photocatalytic performance. In addition, the nanosheets of $Mo_{1-x}S_{2-y}$ become very small (0.111535 $cm^3\ g^{-1}$) after H_2 reduction, but the pore volume (0.157471 $cm^3\ g^{-1}$) is basically constant, which indicates that the electron transfer paths became relatively larger and provided more transfer paths.

Therefore, the mechanism for the ultimate improvement in photocatalytic performance (Scheme 1) can be attributed to the fact that the atomic vibrations of $Mo_{1-x}S_{2-y}$ under H_2-TPR experiment leading to a rearrangement increases the content of the 1T phase, which facilitates the generation of more S vacancies. S vacancies in the 1T phase are produced by the broken Mo-S bond at the phase junction. This leads to the presence of a large amount of free charge inside the lamellae, creating an interlayer built-in electric field that increases the stacking density of $Mo_{1-x}S_{2-y}$ and thus enhances crystallinity. In addition, S vacancies lead to the formation of dangling bonds, which displace atoms and thus curl the lamellae of $Mo_{1-x}S_{2-y}$. The increased energy near the dangling bonds provides more sites for oxygen adsorption. And the small size of the nanosheets due to S vacancies provides abundant channels for
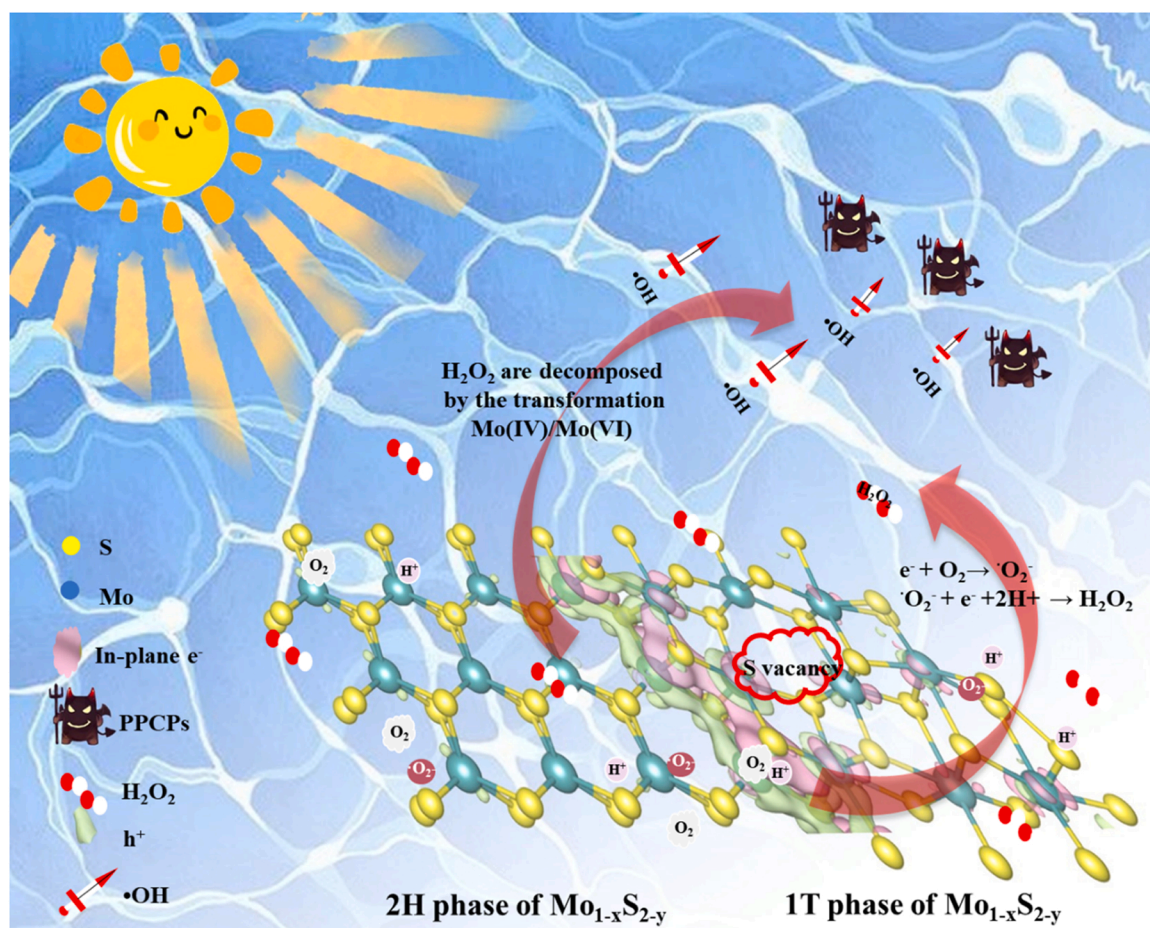
Scheme 1. Mechanism diagram of innergenerate-H_2O_2 production and promotion of pollutant degradation.

electron transfer. The e$^-$ is transferred to the material surface and combined with O_2 in the solution to produce $^\bullet O_2^-$. The $^\bullet O_2^-$ is further reduced and then combined with H$^+$ in the system to increase the yield of H_2O_2. The innergenerate-H_2O_2 then decomposes into undifferentiated aggressive $^\bullet OH$ through the transformation of variable metal Mo atom (Mo(IV)/Mo(VI)). Finally, the $^\bullet OH$ and surplus $^\bullet O_2^-$ attacks contaminants. Thus, high innergenerate-H_2O_2 can effectively degrade pollutants.

4. Conclusion

In conclusion, we have prepared an excellent mixed-phase $Mo_{1-x}S_{2-y}$ photocatalyst with a large number of S vacancies in the 1T phase at the phase-junction using a simple and convenient, low-cost method (H$_2$-TPR). This material can be used for high-efficiency photocatalytic degradation of PPCPs under simulated solar irradiation promoted by innergenerate-H_2O_2. The optimized $Mo_{1-x}S_{2-y}$ photocatalyst has a PPCPs removal performance of 100% in 120 min, and its degradation rate is about twice higher than that of MoS_2. Moreover, the yield of innergenerate-H_2O_2 was up to 35 μmol L^{-1} h^{-1}, which was nearly 1.5 times higher than that of MoS_2. The results verify that S vacancies located in 1T phase at the phase-junction can promote the separation of photo-induced carriers and improve the adsorption of O_2, thus generating $^\bullet O_2^-$. And $^\bullet O_2^-$ further combine excited e$^-$ on the surface of $Mo_{1-x}S_{2-y}$ and H$^+$ in the system to generate innergenerate-H_2O_2. Then the aggressive $^\bullet OH$ is decomposed by H_2O_2 through the transformation of variable metal Mo atom (Mo(IV)/Mo(VI)), thereby boosting the degradation efficiency. This work offers novel and convenient ways and references for the preparation of defective photocatalysts and thus producing H_2O_2 to enhance the degradation of pollutants.

CRediT authorship contribution statement

Xiaojuan Bai: Methodology, Resources, Supervision, Manuscript writing, Writing – review & editing. **Xuyu Wang:** Conceptualization, Data curation, Formal analysis, Investigation, Methodology, Software, Visualization, Roles/Writing – original draft, Experiment and Manuscript writing. **Tianqi Jia:** Investigation. **Linlong Guo:** Investigation. **Derek Hao:** Writing – review & editing, Investigation, Supervision, Contributed to the theoretical analysis. **Ziyang Zhang:** Investigation, Supervision. **Liyuan Wu:** Investigation, Supervision. **Xiaoran Zhang:** Investigation, Supervision. **Hua Yang:** Investigation, Supervision, Discussed the experimental and theoretical. **Yongwei Gong:** Investigation, Supervised the project. **Junqi Li:** Investigation. **Haiyan Li:** Investigation, Supervised the project.

Declaration of Competing Interest

The authors declare that they have no known competing financial interests or personal relationships that could have appeared to influence the work reported in this paper.

Acknowledgments

Appendix A. Supporting information

Supplementary data associated with this article can be found in the online version at doi:10.1016/j.apcatb.2022.121302.

References

[1] O. Baaloudj, I. Assadi, N. Nasrallah, A. El Jery, L. Khezami, A.A. Assadi, Simultaneous removal of antibiotics and inactivation of antibiotic-resistant bacteria by photocatalysis: a review, J. Water Process. Eng. 42 (2021), 102089, https://doi.org/10.1016/j.jwpe.2021.102089.

[2] R.L. Oulton, T. Kohn, D.M. Cwiertny, Pharmaceuticals and personal care products in effluent matrices: a survey of transformation and removal during wastewater treatment and implications for wastewater management, J. Environ. Monit. 12 (2010) 1956–1978, https://doi.org/10.1039/c0em00068j.

[3] Z. Wei, J. Liu, W. Shangguan, A review on photocatalysis in antibiotic wastewater: pollutant degradation and hydrogen production, Chinese, J. Catal. 41 (2020) 1440–1450, https://doi.org/10.1016/s1872-2067(19)63448-0.

[4] S. Wu, Y. Lin, Y.H. Hu, Strategies of tuning catalysts for efficient photodegradation of antibiotics in water environments: a review, J. Mater. Chem. A 9 (2021) 2592–2611, https://doi.org/10.1039/d0ta09173a.

[5] S. Bagheri, A. TermehYousefi, T.-O. Do, Photocatalytic pathway toward degradation of environmental pharmaceutical pollutants: structure, kinetics and mechanism approach, Catal. Sci. Technol. 7 (2017) 4548–4569, https://doi.org/10.1039/c7cy00468k.

[6] X. Yang, Z. Chen, W. Zhao, C. Liu, X. Qian, M. Zhang, G. Wei, E. Khan, Y. Hau Ng, Y. Sik Ok, Recent advances in photodegradation of antibiotic residues in water, Chem. Eng. J. 405 (2021) 126806, https://doi.org/10.1016/j.cej.2020.126806.

[7] Q. Zhu, K. Zhang, D. Li, N. Li, J. Xu, D.W. Bahnemann, C. Wang, Polarization-enhanced photocatalytic activity in non-centrosymmetric materials based photocatalysis: a review, Chem. Eng. J. 426 (2021) 131681, https://doi.org/10.1016/j.cej.2021.131681.

[8] H.-i Kim, Y. Choi, S. Hu, W. Choi, J.-H. Kim, Photocatalytic hydrogen peroxide production by anthraquinone-augmented polymeric carbon nitride, Appl. Catal. B: Environ. 229 (2018) 121–129, https://doi.org/10.1016/j.apcatb.2018.01.060.

[9] Y.N. Xue, P.H. Shao, Y.X. Yuan, W.X. Shi, F.Y. Cui, Activating the basal plane of 2H-MoS$_2$ by doping phosphor for enhancement in the photocatalytic degradation of organic contaminants, ACS Appl. Mater. Interfaces 13 (2021) 38586–38594, https://doi.org/10.1021/acsami.1c08824.

[10] Y. Qin, G. Li, Y. Gao, L. Zhang, Y.S. Ok, T. An, Persistent free radicals in carbon-based materials on transformation of refractory organic contaminants (ROCs) in water: a critical review, Water Res. 137 (2018) 130–143, https://doi.org/10.1016/j.watres.2018.03.012.

[11] T. An, H. Yang, G. Li, W. Song, W.J. Cooper, X. Nie, Kinetics and mechanism of advanced oxidation processes (AOPs) in degradation of ciprofloxacin in water, Appl. Catal. B: Environ. 94 (2010) 288–294, https://doi.org/10.1016/j.apcatb.2009.12.002.

[12] T. An, H. Yang, W. Song, G. Li, H. Luo, W.J. Cooper, Mechanistic considerations for the advanced oxidation treatment of fluoroquinolone pharmaceutical compounds using TiO$_2$ heterogeneous catalysis, J. Phys. Chem. A 114 (2010) 2569–2575, https://doi.org/10.1021/jp911349y.

[13] Y. Liu, Y. Zhu, J. Xu, X. Bai, R. Zong, Y. Zhu, Degradation and mineralization mechanism of phenol by BiPO$_4$ photocatalysis assisted with H$_2$O$_2$, Appl. Catal. B: Environ. 142–143 (2013) 561–567, https://doi.org/10.1016/j.apcatb.2013.05.049.

[14] B. Palanivel, M. Lallimathi, B. Arjunkumar, M. Shkir, T. Alshahrani, K.S. Al-Namshah, M.S. Hamdy, S. Shanavas, M. Venkatachalam, G. Ramalingam, rGO supported g-C$_3$N$_4$/CoFe$_2$O$_4$ heterojunction: Visible-light-active photocatalyst for effective utilization of H$_2$O$_2$ to organic pollutant degradation and •OH radicals production, J. Environ. Chem. Eng. 9 (2021) 104698, https://doi.org/10.1016/j.jece.2020.104698.

[15] C. Li, X. Tan, J. Ma, Concerted high innergenerated-H$_2$O$_2$ photocatalysis and Photo-Fenton degradation of organic pollutants over SCNO@CdS, J. Photochem. Photobiol. A 420 (2021) 113477, https://doi.org/10.1016/j.jphotochem.2021.113477.

[16] Z. Zhou, M. Li, C. Kuai, Y. Zhang, V.F. Smith, F. Lin, A. Aiello, D.P. Durkin, H. Chen, D. Shuai, Fe-based single-atom catalysis for oxidizing contaminants of emerging concern by activating peroxides, J. Hazard. Mater. 418 (2021) 126294, https://doi.org/10.1016/j.jhazmat.2021.126294.

[17] J. Luo, Y. Liu, C. Fan, L. Tang, S. Yang, M. Liu, M. Wang, C. Feng, X. Ouyang, L. Wang, L. Xu, J. Wang, M. Yan, Direct attack and indirect transfer mechanisms dominated by reactive oxygen species for photocatalytic H$_2$O$_2$ production on g-C$_3$N$_4$ possessing nitrogen vacancies, ACS Catal. 11 (2021) 11440–11450, https://doi.org/10.1021/acscatal.1c03103.

[18] H. Song, L. Wei, C. Chen, C. Wen, F. Han, Photocatalytic production of H$_2$O$_2$ and its in situ utilization over atomic-scale Au modified MoS$_2$ nanosheets, J. Catal. 376 (2019) 198–208, https://doi.org/10.1016/j.jcat.2019.06.015.

[19] X. Wei, H. Yi, C. Lai, X. Huo, D. Ma, C. Du, Synergistic effect of flower-like MnFe$_2$O$_4$/MoS$_2$ on photo-Fenton oxidation remediation of tetracycline polluted water, J. Colloid Interface Sci. 608 (2022) 942–953, https://doi.org/10.1016/j.jcis.2021.10.033.

[20] J. Liu, C. Dong, Y. Deng, J. Ji, S. Bao, C. Chen, B. Shen, J. Zhang, M. Xing, Molybdenum sulfide Co-catalytic fenton reaction for rapid and efficient inactivation of Escherichia coli, Water Res. 145 (2018) 312–320, https://doi.org/10.1016/j.watres.2018.08.039.

[21] J. Ma, K. Wang, C. Wang, X. Chen, W. Zhu, G. Zhu, W. Yao, Y. Zhu, Photocatalysis-self-Fenton system with high-fluent degradation and high mineralization ability, Appl. Catal. B: Environ. 276 (2020) 119150, https://doi.org/10.1016/j.apcatb.2020.119150.

[22] Y. Wu, J. Chen, H. Che, X. Gao, Y. Ao, P. Wang, Boosting 2e$^-$ oxygen reduction reaction in garland carbon nitride with carbon defects for high-efficient

photocatalysis-self-Fenton degradation of 2,4-dichlorophenol, Appl. Catal. B: Environ. 307 (2022), 121185, https://doi.org/10.1016/j.apcatb.2022.121185.

[23] H. Che, X. Gao, J. Chen, J. Hou, Y. Ao, P. Wang, Iodide-induced fragmentation of polymerized hydrophilic carbon nitride for high-performance quasi-homogeneous photocatalytic H_2O_2 production, Angew. Chem. Int. Ed. 60 (2021) 25546–25550, https://doi.org/10.1002/anie.202111769.

[24] Y. Shiraishi, Y. Ueda, A. Soramoto, S. Hinokuma, T. Hirai, Photocatalytic hydrogen peroxide splitting on metal-free powders assisted by phosphoric acid as a stabilizer, Nat. Commun. 11 (2020) 3386, https://doi.org/10.1038/s41467-020-17216-2.

[25] X. Hu, X. Zeng, Y. Liu, J. Lu, S. Yuan, Y. Yin, J. Hu, D.T. McCarthy, X. Zhang, Nano-layer based 1T-rich MoS_2/g-C_3N_4 co-catalyst system for enhanced photocatalytic and photoelectrochemical activity, Appl. Catal. B: Environ. 268 (2020), 118466, https://doi.org/10.1016/j.apcatb.2019.118466.

[26] D. Voiry, R. Fullon, J. Yang, E.S.C. de Carvalho Castro, R. Kappera, I. Bozkurt, D. Kaplan, M.J. Lagos, P.E. Batson, G. Gupta, A.D. Mohite, L. Dong, D. Er, V. B. Shenoy, T. Asefa, M. Chhowalla, The role of electronic coupling between substrate and 2D MoS_2 nanosheets in electrocatalytic production of hydrogen, Nat. Mater. 15 (2016) 1003–1009, https://doi.org/10.1038/nmat4660.

[27] Y. Liu, Y. Li, F. Peng, Y. Lin, S. Yang, S. Zhang, H. Wang, Y. Cao, H. Yu, 2H- and 1T-mixed phase few-layer MoS_2 as a superior to Pt co-catalyst coated on TiO_2 nanorod arrays for photocatalytic hydrogen evolution, Appl. Catal. B: Environ. 241 (2019) 236–245, https://doi.org/10.1016/j.apcatb.2018.09.040.

[28] Q. Li, N. Zhang, Y. Yang, G. Wang, D.H. Ng, High efficiency photocatalysis for pollutant degradation with MoS_2/C_3N_4 heterostructures, Langmuir 30 (2014) 8965–8972, https://doi.org/10.1021/la502033t.

[29] Z. Li, R. Ye, R. Feng, Y. Kang, X. Zhu, J.M. Tour, Z. Fang, Graphene quantum dots doping of MoS_2 monolayers, Adv. Mater. 27 (2015) 5235–5240, https://doi.org/10.1002/adma.201501888.

[30] D. Wang, Y. Xiao, X. Luo, Z. Wu, Y.-J. Wang, B. Fang, Swollen ammoniated MoS_2 with 1T/2H hybrid phases for high-rate electrochemical energy storage, ACS Sustain. Chem. Eng. 5 (2017) 2509–2515, https://doi.org/10.1021/acssuschemeng.6b02863.

[31] Y. Zhang, Y. Kuwahara, K. Mori, H. Yamashita, Defect engineering of MoS_2 and its impacts on electrocatalytic and photocatalytic behavior in hydrogen evolution reactions, Chem. Asian J. 14 (2019) 278–285, https://doi.org/10.1002/asia.201801594.

[32] Y. Fang, X. Hu, W. Zhao, J. Pan, D. Wang, K. Bu, Y. Mao, S. Chu, P. Liu, T. Zhai, F. Huang, Structural determination and nonlinear optical properties of new 1T'''-Type MoS_2 compound, J. Am. Chem. Soc. 141 (2019) 790–793, https://doi.org/10.1021/jacs.8b12133.

[33] W. Ding, L. Hu, J. Dai, X. Tang, R. Wei, Z. Sheng, C. Liang, D. Shao, W. Song, Q. Liu, M. Chen, X. Zhu, S. Chou, X. Zhu, Q. Chen, Y. Sun, S.X. Dou, Highly ambient-stable 1T-MoS_2 and 1T-WS_2 by hydrothermal synthesis under high magnetic fields, ACS Nano 13 (2019) 1694–1702, https://doi.org/10.1021/acsnano.8b07744.

[34] L. Zhang, L. Mu, Q. Zhou, X. Hu, Solar-assisted fabrication of dimpled 2H-MoS_2 membrane for highly efficient water desalination, Water Res. 170 (2020), 115367, https://doi.org/10.1016/j.watres.2019.115367.

[35] W. Peng, Y. Li, F. Zhang, G. Zhang, X. Fan, Roles of two-dimensional transition metal dichalcogenides as cocatalysts in photocatalytic hydrogen evolution and environmental remediation, Ind. Eng. Chem. Res. 56 (2017) 4611–4626, https://doi.org/10.1021/acs.iecr.7b00371.

[36] Z. Wang, B. Mi, Environmental applications of 2D molybdenum disulfide (MoS_2) nanosheets, Environ. Sci. Technol. 51 (2017) 8229–8244, https://doi.org/10.1021/acs.est.7b01466.

[37] Y. Chen, G. Zhang, Q. Ji, H. Liu, J. Qu, Triggering of low-valence molybdenum in multiphasic MoS_2 for effective reactive oxygen species output in catalytic Fenton-like reactions, ACS Appl. Mater. Interfaces 11 (2019) 26781–26788, https://doi.org/10.1021/acsami.9b05978.

[38] K. Le, X. Zhang, Q. Zhao, Y. Liu, P. Yi, S. Xu, W. Liu, Controllably doping nitrogen into 1T/2H MoS_2 heterostructure nanosheets for enhanced supercapacitive and electrocatalytic performance by low-power N_2 plasma, ACS Appl. Mater. Interfaces 13 (2021) 44427–44439, https://doi.org/10.1021/acsami.1c12973.

[39] Z.W. Seh, J. Kibsgaard, C.F. Dickens, I. Chorkendorff, J.K. Norskov, T.F. Jaramillo, Combining theory and experiment in electrocatalysis: insights into materials design, Science 355 (2017) 6321, https://doi.org/10.1126/science.aad4998.

[40] Q. Li, B. Hu, Q. Yang, X. Cai, M. Nie, Y. Jin, L. Zhou, Y. Xu, Q. Pan, L. Fang, Interaction mechanism between multi-layered MoS_2 and H_2O_2 for self-generation of reactive oxygen species, Environ. Res. 191 (2020), 110227, https://doi.org/10.1016/j.envres.2020.110227.

[41] Z. Liu, Z. Gao, Y. Liu, M. Xia, R. Wang, N. Li, Heterogeneous nanostructure based on 1T-phase MoS_2 for enhanced electrocatalytic hydrogen evolution, ACS Appl. Mater. Interfaces 9 (2017) 25291–25297, https://doi.org/10.1021/acsami.7b05775.

[42] H. Zhou, L. Lai, Y. Wan, Y. He, G. Yao, B. Lai, Molybdenum disulfide (MoS_2): a versatile activator of both peroxymonosulfate and persulfate for the degradation of carbamazepine, Chem. Eng. J. 384 (2020), 123264, https://doi.org/10.1016/j.cej.2019.123264.

[43] Y. Cao, Roadmap and direction toward high-performance MoS_2 hydrogen evolution catalysts, ACS Nano 15 (2021) 11014–11039, https://doi.org/10.1021/acsnano.1c01879.

[44] R. Shi, Y. Zhao, G.I.N. Waterhouse, S. Zhang, T. Zhang, Defect engineering in photocatalytic nitrogen fixation, ACS Catal. 9 (2019) 9739–9750, https://doi.org/10.1021/acscatal.9b03246.

[45] N. Luo, C. Chen, D. Yang, W. Hu, F. Dong, S defect-rich ultrathin 2D MoS_2: the role of S point-defects and S stripping-defects in the removal of Cr(VI) via synergistic

[46] adsorption and photocatalysis, Appl. Catal. B: Environ. 299 (2021), 120664, https://doi.org/10.1016/j.apcatb.2021.120664.

[46] Y. Peng, M. Geng, J. Yu, Y. Zhang, F. Tian, Yn Guo, D. Zhang, X. Yang, Z. Li, Z. Li, S. Zhang, Vacancy-induced 2H@1T MoS_2 phase-incorporation on $ZnIn_2S_4$ for boosting photocatalytic hydrogen evolution, Appl. Catal. B: Environ. 298 (2021), 120570, https://doi.org/10.1016/j.apcatb.2021.120570.

[47] X. Li, W. Wang, F. Dong, Z. Zhang, L. Han, X. Luo, J. Huang, Z. Feng, Z. Chen, G. Jia, T. Zhang, Recent advances in noncontact external-field-assisted photocatalysis: from fundamentals to applications, ACS Catal. 11 (2021) 4739–4769, https://doi.org/10.1021/acscatal.0c05354.

[48] J. Luo, S. Zhang, M. Sun, L. Yang, S. Luo, J.C. Crittenden, A critical review on energy conversion and environmental remediation of photocatalysts with remodeling crystal lattice, surface, and interface, ACS Nano 13 (2019) 9811–9840, https://doi.org/10.1021/acsnano.9b03649.

[49] L.N. Zhou, D.F. Swearer, C. Zhang, H. Robatjazi, H.Q. Zhao, L. Henderson, L. L. Dong, P. Christopher, E.A. Carter, P. Nordlander, N.J. Halas, Quantifying hot carrier and thermal contributions in plasmonic photocatalysis, Science 362 (2018) 69–72, https://doi.org/10.1126/science.aat6967.

[50] N. Dinter, M. Rusanen, P. Raybaud, S. Kasztelan, Pd Silva, H. Toulhoat, Temperature-programed reduction of unpromoted MoS_2-based hydrodesulfurization catalysts: experiments and kinetic modeling from first principles, J. Catal. 267 (2009) 67–77, https://doi.org/10.1016/j.jcat.2009.07.017.

[51] H. Cao, Z. Bai, Y. Li, Z. Xiao, X. Zhang, G. Li, Solvothermal synthesis of defect-rich mixed 1T–2H MoS_2 nanoflowers for enhanced hydrodesulfurization, ACS Sustain. Chem. Eng. 8 (2020) 7343–7352, https://doi.org/10.1021/acssuschemeng.0c00736.

[52] M. Sreeramareddygari, J. Mannekote Shivanna, M. Somasundrum, K. Soontarapa, W. Surareungchai, Polythiocyanuric acid-functionalized MoS_2 nanosheet-based high flux membranes for removal of toxic heavy metal ions and Congo red, Chem. Eng. J. 425 (2021), 130592, https://doi.org/10.1016/j.cej.2021.130592.

[53] D. Tang, J. Li, Z. Yang, X. Jiang, L. Huang, X. Guo, Y. Li, J. Zhu, S. Sun, Fabrication and mechanism exploration of oxygen-incorporated 1T-MoS_2 with high adsorption performance on methylene blue, Chem. Eng. J. 428 (2022), 130954, https://doi.org/10.1016/j.cej.2021.130954.

[54] M. Dan, J. Xiang, F. Wu, S. Yu, Q. Cai, L. Ye, Y. Ye, Y. Zhou, Rich active-edge-site MoS_2 anchored on reduction sites in metal sulfide heterostructure: toward robust visible light photocatalytic hydrogen sulphide splitting, Appl. Catal. B: Environ. 256 (2019), 117870, https://doi.org/10.1016/j.apcatb.2019.117870.

[55] S.J. Rathi, A.K. Ray, On the existence and stability of single walled SiGe nanotubes, Chem. Phys. Lett. 466 (2008) 79–83, https://doi.org/10.1016/j.cplett.2008.10.031.

[56] J. Wei, P. He, J. Wu, N. Chen, T. Xu, E. Shi, C. Pan, X. Zhao, Y. Zhang, Conversion of 2H MoS_2 to 1T MoS_2 via lithium ion doping: Effective removal of elemental mercury, Chem. Eng. J. 428 (2022), 131014, https://doi.org/10.1016/j.cej.2021.131014.

[57] C. Tian, B. Li, X. Hu, J. Wu, P. Li, X. Xiang, X. Zu, S. Li, Melamine foam derived 2H/1T MoS_2 as flexible interlayer with efficient polysulfides trapping and fast Li(+) diffusion to stabilize Li-S batteries, ACS Appl. Mater. Interfaces 13 (2021) 6229–6240, https://doi.org/10.1021/acsami.0c19725.

[58] Y. Wang, F. Lu, K. Su, N. Zhang, Y. Zhang, M. Wang, X. Wang, Engineering Mo-O-C interface in MoS_2@rGO via charge transfer boosts hydrogen evolution, Chem. Eng. J. 399 (2020), 126018, https://doi.org/10.1016/j.cej.2020.126018.

[59] Y. Zhang, Y. Kuwahara, K. Mori, C. Louis, H. Yamashita, Hybrid phase 1T/2H-MoS_2 with controllable 1T concentration and its promoted hydrogen evolution reaction, Nanoscale 12 (2020) 11908–11915, https://doi.org/10.1039/d0nr02525a.

[60] X. Bai, X. Wang, X. Lu, Y. Liang, J. Li, L. Wu, H. Li, Q. Hao, B.J. Ni, C. Wang, Surface defective g-$C_3N_{4-x}Cl_x$ with unique spongy structure by polarization effect for enhanced photocatalytic removal of organic pollutants, J. Hazard. Mater. 398 (2020), 122897, https://doi.org/10.1016/j.jhazmat.2020.122897.

[61] W. Qiao, W. Xu, X. Xu, L. Wu, S. Yan, D. Wang, Construction of active orbital via single-atom cobalt anchoring on the surface of 1T-MoS_2 basal plane toward efficient hydrogen evolution, ACS Appl. Energy Mater. 3 (2020) 2315–2322, https://doi.org/10.1021/acsaem.0c00163.

[62] C. Zhu, Q. Xian, Q. He, C. Chen, W. Zou, C. Sun, S. Wang, X. Duan, Edge-rich bicrystalline 1T/2H-MoS_2 cocatalyst-decorated {110} terminated CeO_2 nanorods for photocatalytic hydrogen evolution, ACS Appl. Mater. Interfaces 13 (2021) 35818–35827, https://doi.org/10.1021/acsami.1c09651.

[63] S. Kumari, A. Chouhan, O.P. Sharma, S. Kuriakose, S.A. Tawfik, M.J.S. Spencer, S. Walia, H. Sugimura, O.P. Khatri, Structural-defect-mediated grafting of alkylamine on few-layer MoS_2 and its potential for enhancement of tribological properties, ACS Appl. Mater. Interfaces 12 (2020) 30720–30730, https://doi.org/10.1021/acsami.0c08307.

[64] L. Cai, W. Cheng, T. Yao, Y. Huang, F. Tang, Q. Liu, W. Liu, Z. Sun, F. Hu, Y. Jiang, W. Yan, S. Wei, High-content metallic 1T phase in MoS_2-based electrocatalyst for efficient hydrogen evolution, J. Phys. Chem. C 121 (2017) 15071–15077, https://doi.org/10.1021/acs.jpcc.7b03103.

[65] K.-K. Liu, W.J. Zhang, Y.-H. Lee, Y.-C. Lin, M.-T. Chang, C.-Y. Su, C.-S. Chang, H. Li, Y.M. Shi, H. Zhang, C.-S. Lai, L.-J. Li, Growth of large-area and highly crystalline MoS_2 thin layers oninsulating substrates, Nano Lett. 12 (2012) 1538–1544, https://doi.org/10.1021/nl2043612.

[66] S. Khan, H. Cho, D. Kim, S.S. Han, K.H. Lee, S.-H. Cho, T. Song, H. Choi, Defect engineering toward strong photocatalysis of Nb-doped anatase TiO_2: computational predictions and experimental verifications, Appl. Catal. B: Environ. 206 (2017) 520–530, https://doi.org/10.1016/j.apcatb.2017.01.039.

[67] X. Zou, Z. Zhang, X. Chen, B.I. Yakobson, Structure and dynamics of the electronic heterointerfaces in MoS$_2$ by first-principles simulations, J. Phys. Chem. Lett. 11 (2020) 1644–1649, https://doi.org/10.1021/acs.jpclett.0c00147.

[68] C. Pipitone, S. Carlotto, M. Casarin, A. Longo, A. Martorana, F. Giannici, Bi^{3+} doping in 1D ((CH$_3$)$_3$SO)PbI$_3$: a model for defect interactions in halide perovskites, J. Mater. Chem. C. 10 (2022) 1458–1469, https://doi.org/10.1039/d1tc05057e.

[69] S. Wang, D. Zhang, B. Li, C. Zhang, Z. Du, H. Yin, X. Bi, S. Yang, Ultrastable in-plane 1T–2H MoS$_2$ heterostructures for enhanced hydrogen evolution reaction, Adv. Energy Mater. 8 (2018), 1801345, https://doi.org/10.1002/aenm.201801345.

[70] J. Xi, H. Xia, X. Ning, Z. Zhang, J. Liu, Z. Mu, S. Zhang, P. Du, X. Lu, Carbon-intercalated 0D/2D hybrid of hematite quantum dots/graphitic carbon nitride nanosheets as superior catalyst for advanced oxidation, Small 15 (2019), 1902744, https://doi.org/10.1002/smll.201902744.

[71] Y. Shi, D. Zheng, X. Zhang, K. Lv, F. Wang, B. Dong, S. Wang, C. Yang, J. Li, F. Yang, L.Y. Hao, L. Yin, X. Xu, Y. Xian, S. Agathopoulos, Self-supported ceramic electrode of 1T–2H MoS$_2$ grown on the TiC membrane for hydrogen production, Chem. Mater. 33 (2021) 6217–6226, https://doi.org/10.1021/acs.chemmater.1c01965.

[72] X. Bai, X. Wang, X. Lu, S. Hou, B. Sun, C. Wang, T. Jia, S. Yang, High crystallinity and conjugation promote the polarization degree in O-doped g-C$_3$N$_4$ for removing organic pollutants, CrystEngComm 23 (2021) 1366–1376, https://doi.org/10.1039/d0ce01776k.

[73] H. Li, C. Wang, X. Bai, X. Wang, B. Sun, D. Li, L. Zhao, R. Zong, D. Hao, In-plane polarization induced by the hydrogen bonding and π–π stacking of functionalized PDI supramolecules for the efficient photocatalytic degradation of organic pollutants, Mater. Chem. Front. 4 (2020) 2673–2687, https://doi.org/10.1039/d0qm00349b.

[74] G. Li, Z. Yi, H. Wang, C. Jia, W. Zhang, Factors impacted on anisotropic photocatalytic oxidization activity of ZnO: surface band bending, surface free energy and surface conductance, Appl. Catal. B: Environ. 158–159 (2014) 280–285, https://doi.org/10.1016/j.apcatb.2014.04.034.

[75] X. Du, J. Wan, J. Jia, C. Pan, X. Hu, J. Fan, E. Liu, Photocatalystic degradation of RhB over highly visible-light-active Ag$_3$PO$_4$-Bi$_2$MoO$_6$ heterojunction using H$_2$O$_2$ electron capturer, Mater. Des. 119 (2017) 113–123, https://doi.org/10.1016/j.matdes.2017.01.070.

[76] S. Tiwari, S. Kumar, A.K. Ganguli, Role of MoS$_2$/rGO co-catalyst to enhance the activity and stability of Cu$_2$O as photocatalyst towards photoelectrochemical water splitting, J. Photochem. Photobiol. A: Chem. 424 (2022), 113622, https://doi.org/10.1016/j.jphotochem.2021.113622.

[77] R. Zhou, S. Yang, T. E, L. Liu, J. Qian, The defect is perfect: MoS$_2$/TiO$_2$ modified with unsaturated Mo vacancies to construct Z-scheme heterojunction & improve mobility of e$^-$, J. Clean. Prod. 337 (2022), 130511, https://doi.org/10.1016/j.jclepro.2022.130511.

[78] C. Sun, F. Li, J. Ren, J. Wu, G. Wang, L. Chen, Photocatalytic H$_2$ production with simultaneous wastewater purification over flower-like 1T/2H-MoS$_2$-decorated CNT/CNU isotype heterojunction photocatalyst, Appl. Surf. Sci. 569 (2021), 151072, https://doi.org/10.1016/j.apsusc.2021.151072.

[79] L. Jiang, Y.-J. Zhang, X.-H. Luo, L. Yu, H.-X. Li, Y.-J. Li, Se and O co-insertion induce the transition of MoS$_2$ from 2H to 1T phase for designing high-active electrocatalyst of hydrogen evolution reaction, Chem. Eng. J. 425 (2021), 130611, https://doi.org/10.1016/j.cej.2021.130611.

[80] X. Zhang, F. Tian, X. Lan, Y. Liu, W. Yang, J. Zhang, Y. Yu, Building P-doped MoS$_2$/g-C$_3$N$_4$ layered heterojunction with a dual-internal electric field for efficient photocatalytic sterilization, Chem. Eng. J. 429 (2022), 132588, https://doi.org/10.1016/j.cej.2021.132588.

[81] S. Das, R. Ghosh, P. Routh, A. Shit, S. Mondal, A. Panja, A.K. Nandi, Conductive MoS$_2$ quantum Dot/Polyaniline aerogel for enhanced electrocatalytic hydrogen evolution and photoresponse properties, ACS Appl. Nano Mater. 1 (2018) 2306–2316, https://doi.org/10.1021/acsanm.8b00373.

[82] S. Zang, G. Zhang, Z.-A. Lan, D. Zheng, X. Wang, Enhancement of photocatalytic H$_2$ evolution on pyrene-based polymer promoted by MoS$_2$ and visible light, Appl. Catal. B: Environ. 251 (2019) 102–111, https://doi.org/10.1016/j.apcatb.2019.03.061.

[83] A. Bar-Hen, R. Bar-Ziv, T. Ohaion-Raz, A. Mizrahi, S. Hettler, R. Arenal, M. Bar Sadan, Shelling with MoS$_2$: functional CuS@MoS$_2$ hybrids as electrocatalysts for the oxygen reduction and hydrogen evolution reactions, Chem. Eng. J. 420 (2021), 129771, https://doi.org/10.1016/j.cej.2021.129771.

[84] R. Bardestani, G.S. Patience, S. Kaliaguine, Experimental methods in chemical engineering: specific surface area and pore size distribution measurements—BET, BJH, and DFT, Can. J. Chem. Eng. 97 (2019) 2781–2791, https://doi.org/10.1002/cjce.23632.

[85] Y. Li, X. Xing, J. Pei, R. Li, Y. Wen, S. Cui, T. Liu, Automobile exhaust gas purification material based on physical adsorption of tourmaline powder and visible light catalytic decomposition of g-C$_3$N$_4$/BiVO$_4$, Ceram. Int. 46 (2020) 12637–12647, https://doi.org/10.1016/j.ceramint.2020.02.029.